Nano Research

Open Access

Research Article

Protonated layered titanate anode at 0.008 V enables 1.75 V rocking-chair aqueous zinc-ion batteries with 87% energy efficiency

Xinyu Guo[1], Yan Chen[1], Yi Zhou[1], Jinke Li[1], Pu He[1], Ying Tang[1], Wenjun Deng[2] ✉, and Rui Li[1] ✉

[1] *School of Advanced Materials, Peking University Shenzhen Graduate School, Shenzhen 518055, China*
[2] *School of Materials and Environmental Engineering, Shenzhen Polytechnic University, Shenzhen 518055, China*

Cite this article: *Nano Research*, **2026**, *19*, 94908435. https://doi.org/10.26599/NR.2026.94908435

ABSTRACT: Aqueous zinc-ion batteries (AZIBs) with metallic Zn anodes face significant challenges, including dendrite growth, low Zn utilization, and parasitic side reactions. Inspired by rocking-chair design of lithium-ion batteries, developing intercalative anodes offers a promising strategy to address these issues. However, existing anode materials exhibit limited diversity, high redox potentials (≥ 0.3 V vs. Zn^{2+}/Zn), and low energy efficiency, constraining the development of rocking-chair zinc-ion batteries. Herein, we report protonated layered titanate ($H_2Ti_3O_7$) that demonstrates an ultra-low redox potential of 0.008 V vs. Zn^{2+}/Zn. The anode delivers a reversible capacity of 78 mAh·g^{-1} at 0.2 A·g^{-1}, along with superior rate performance and remarkable cycling stability. *In situ* X-ray diffraction (XRD) analysis reveals a two-phase reaction mechanism during Zn^{2+} (de)intercalation. When coupled with a zinc hexacyanoferrate (KZnHCF) cathode, the full cell achieves a high output voltage of 1.75 V, long-term cycling stability of 3000 cycles, and an exceptional energy efficiency of 87% that far exceeds commercial lead-acid batteries. This work provides a highly promising anode candidate for the realization of high-voltage, high-energy-efficiency, and dendrite-free AZIBs.

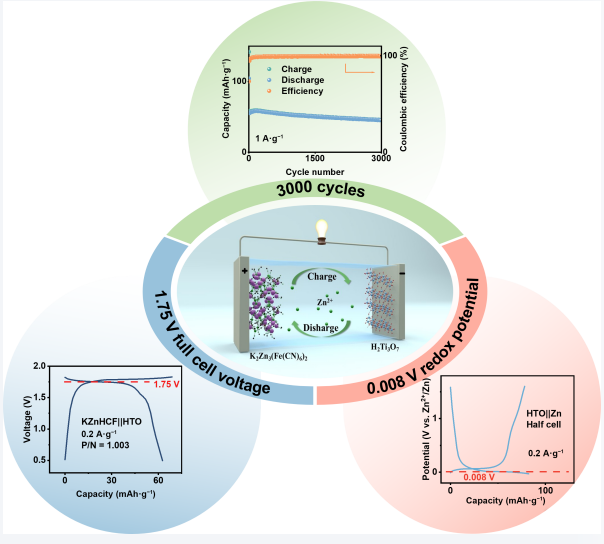

KEYWORDS: hydrated titanic acid, aqueous zinc-ion batteries, zinc metal-free anode, "rocking-chair" type

1 Introduction

Aqueous zinc-ion batteries (AZIBs) have garnered significant attention owing to their economic feasibility, low cost, and environmental benignancy [1, 2]. However, the advancement of AZIBs with metal Zn anodes is hindered by several critical challenges, including uncontrolled Zn dendrite growth, extremely low Zn utilization (< 5%), and detrimental side reactions, such as corrosion and hydrogen evolution [3–6]. These issues collectively result in a limited lifespan, inadequate practical capacity, and energy density, thereby impeding their commercialization.

Leveraging the successful commercialization of lithium-ion batteries, where the replacement of Li metal with the intercalated graphite material as the anode electrode effectively mitigates the issue of lithium dendrite formation, a promising strategy to address the aforementioned challenges in AZIBs is the rational design of metal-free rocking-chair AZIBs, which enables reversible zinc-ion (de)intercalation between the cathode and anode [7–9]. This approach not only prevents the formation of zinc dendrites but also suppresses undesired corrosion reactions [10–12]. To date, the development of intercalated anodes for AZIBs remains in its infancy, with only a restricted number of materials having been developed. Despite the enhanced cycling performance, most of the intercalated anodes demonstrate a high output potential (≥ 0.3 V vs. Zn^{2+}/Zn), restricting the output voltage of the full battery [13–17]. The limited output voltage significantly affects practical utilization by not only reducing energy density but also substantially decreasing energy efficiency (EE). This underscores the urgent need to explore anodes with low Zn^{2+} intercalation potential.

Ti-based materials featuring Ti^{3+}/Ti^{4+} redox couples exhibit

Received: October 15, 2025; **Revised:** December 22, 2025
Accepted: January 13, 2026

✉Address correspondence to Wenjun Deng, dengwenjun@szpu.edu.cn; Rui Li, liruisz@pku.edu.cn

relatively low potentials, making them highly promising candidates as the anode materials for metal-free AZIBs. For instance, $Na_{0.14}TiS_2$ delivers a capacity of 140 mAh·g^{-1} with a discharge voltage of 0.3 V vs. Zn^{2+}/Zn [18], $H_2Ti_3O_7$-MXene shows a low charging voltage of only 0.25 V vs. Zn^{2+}/Zn [19], and $H_2Ti_3O_7{\cdot}xH_2O$ exhibited a low redox potential of approximately 0.2 V vs. Zn^{2+}/Zn [20]. Recently, our group reported two different types of titanium phosphate, $Ti_2O(PO_4)_2{\cdot}2H_2O$ and $Ti_2O_3(H_2PO_4)_2{\cdot}2H_2O$, demonstrating depressed potentials of 0.07 and 0.17 V vs. Zn^{2+}/Zn, respectively [21, 22]. However, the development of Ti-based intercalative anodes for AZIBs remains challenging due to limited material options, inadequate rate performance, and low energy efficiency. Therefore, rational anode design is of critical importance to achieve a Zn^{2+} intercalation potential that is as low as possible while maintaining favorable Zn^{2+} transport kinetics.

In this work, we report another Ti-based anode material, hydrated titanic acid ($H_2Ti_3O_7$, named HTO) with an ultra-low redox potential of 0.008 V vs. Zn^{2+}/Zn, which represents the lowest intercalation potential ever reported for "rocking-chair" AZIBs anode materials to the best of our knowledge. This HTO anode delivers a reversible capacity of 78 mAh·g^{-1} at 0.2 A·g^{-1} and maintains 90.6% of its initial capacity after 1000 cycles at 1 A·g^{-1}, indicating excellent cycling stability. Additionally, it exhibits superior rate capability, retaining 66% of its capacity at a high current density of 2.0 A·g^{-1}. Moreover, in contrast to the previously reported single-phase solid solution reaction of HTO in AZIBs [20], this study identifies the occurrence of a two-phase transformation reaction for the first time, as evidenced by the *in situ* X-ray diffraction (XRD) executed during the electrochemical process. When coupled with zinc hexacyanoferrate (KZnHCF) cathode, the full cell exhibits a high output voltage of 1.75 V and a stable cycling property of 78.5% capacity retention after 3000 cycles at 1 A·g^{-1}. More importantly, an impressive energy efficiency of 87% is achieved, which is the highest among "rocking-chair" AZIBs to our knowledge and even surpasses commercial lead-acid batteries, underscoring its promising potential for practical applications.

2 Results and discussion

2.1 Characterizations of HTO

$H_2Ti_3O_7$ was synthesized from $Na_2Ti_3O_7$ (named NTO), which served as the parent compound. NTO was first prepared via solid-state sintering, and HTO was subsequently obtained through a Na^+/H^+ ion exchange process carried out in hydrochloric acid solution, as illustrated in Fig. 1(a) [23, 24]. The detailed synthesis procedure is provided in Section 4. The HTO structure consists of corrugated layers composed of edge-sharing TiO_6 octahedra, forming negatively charged $(Ti_3O_7)^{2-}$ anionic layers, with protons residing in the interlayer galleries [24]. This layered structure renders HTO an ideal host material for ion intercalation [25]. Figure 1(b) presents the XRD patterns of NTO and HTO, which are in good agreement with the reference patterns of monoclinic $Na_2Ti_3O_7$ (PDF#72-0148) and $H_2Ti_3O_7$ (PDF#47-0561), respectively, indicating the successful synthesis of single-phase layered materials with high crystallinity. Rietveld refinement of the XRD pattern for HTO was conducted, as shown in Fig. S1 in the Electronic Supplementary Material (ESM). The Rietveld refinement shows that the synthesized material is mainly composed of predominant $H_2Ti_3O_7$ phase (90.3%), with a small amount of $Na_2Ti_3O_7$ phase remaining (9.7%), confirming the successful synthesis of HTO through the ion-exchange process. The structure of $Na_2Ti_3O_7$ phase is monoclinic, space group $P2_1/m$, with lattice parameters of a = 8.25674 Å, b = 3.85845 Å, c = 9.56673 Å, α = 90°, β = 106.2284°, and γ = 90°. The structure of $H_2Ti_3O_7$ phase is monoclinic, space group $C2/m$, with lattice parameters of a = 16.03889 Å, b = 3.74670 Å, c = 9.19124 Å, α = 90°, β = 101.5751°, and γ = 90°. The reliability factors reach profile residual (R_p) = 8.5%, weighted profile residual (R_{wp}) = 11.88%, and goodness of fit (χ^2) = 6.27.

X-ray photoelectron spectroscopy (XPS) was employed to investigate the surface chemical composition of NTO and HTO. The full XPS spectra are presented in Fig. S2 in the ESM, while the high-resolution XPS spectra of Na 1s and O 1s are shown in Fig. 1(c) and Fig. S3 in the ESM, respectively. As illustrated in Fig. 1(c), the intensity of the Na 1s characteristic peak decreases significantly after the ion exchange process, indicating that the majority of sodium was effectively removed in HTO. The O 1s spectra in Fig. S3 in the ESM further support this conclusion, as the peak at 535 eV that corresponds to the Na KLL Auger peak is no longer present in the HTO spectrum, confirming minimal residual sodium [26–28]. Figure S4 in the ESM shows the thermogravimetry analysis (TGA) curve of HTO powder, which was carried out under a N_2 atmosphere from room temperature to 800 °C. A total weight loss of 6.275% is observed, corresponding to the loss of interlayer protons and crystalline water. Inductively coupled plasma optical emission spectrometry (ICP-OES) was also performed, revealing an atomic ratio of Na/Ti of 0.049 (Table S1 in the ESM). Figure 1(d) presents the Raman spectra of NTO and HTO materials, where the peaks in the range of 700 to 900 cm^{-1} can be attributed to the Ti–O stretching modes [29, 30]. Two distinct peaks located at 774 and 845 cm^{-1} are observed in the Raman spectrum of HTO, indicating the presence of two different bonding environments associated with terminal and bridging oxygen atoms, respectively [31]. In addition, a noticeable shift in the positions of these Ti–O stretching modes is observed after the Na^+/H^+ ion exchange process, changing from 850 and 885 cm^{-1} to 774 and 845 cm^{-1}, respectively, suggesting the weaker Ti–O bonds in HTO compared to those in NTO [30]. This shift may result from a transition in bonding character from ionic to covalent as sodium ions are replaced by protons [31].

Figure S5 in the ESM and Fig. 1(e) show the scanning electron microscopy (SEM) images of NTO and HTO, respectively. Both materials exhibit a micro rod-like morphology, suggesting the Na^+/H^+ ion exchange process in hydrochloric acid solution does not alter the morphology of the material. Energy dispersive spectroscopy (EDS) analysis was also conducted, as shown in Fig. S6 in the ESM, demonstrating that the atomic ratio of Na in HTO decreases to 1.1%, compared to 14.9% in the pristine NTO, which is aligned with the ICP results. The high-resolution transmission electron microscopy (HRTEM) image (Fig. 1(f)) reveals distinct lattice fringes with d-spacings of 0.78 and 0.33 nm, corresponding to the (200) and (40$\bar{2}$) planes of HTO, respectively. Furthermore, the selected area electron diffraction (SAED) pattern along the [$\bar{1}$114] zone axis exhibits clear and well-organized diffraction spots (Fig. 1(g)), which can be indexed to the (31$\bar{2}$), (401), (1$\bar{1}$3), and ($\bar{7}$11) planes of HTO, respectively.

2.2 Electrochemical performance of the HTO anode

The Zn^{2+} storage performance of HTO was evaluated in a half-cell with Zn foil as the anode, HTO electrode as the cathode, glass-fiber

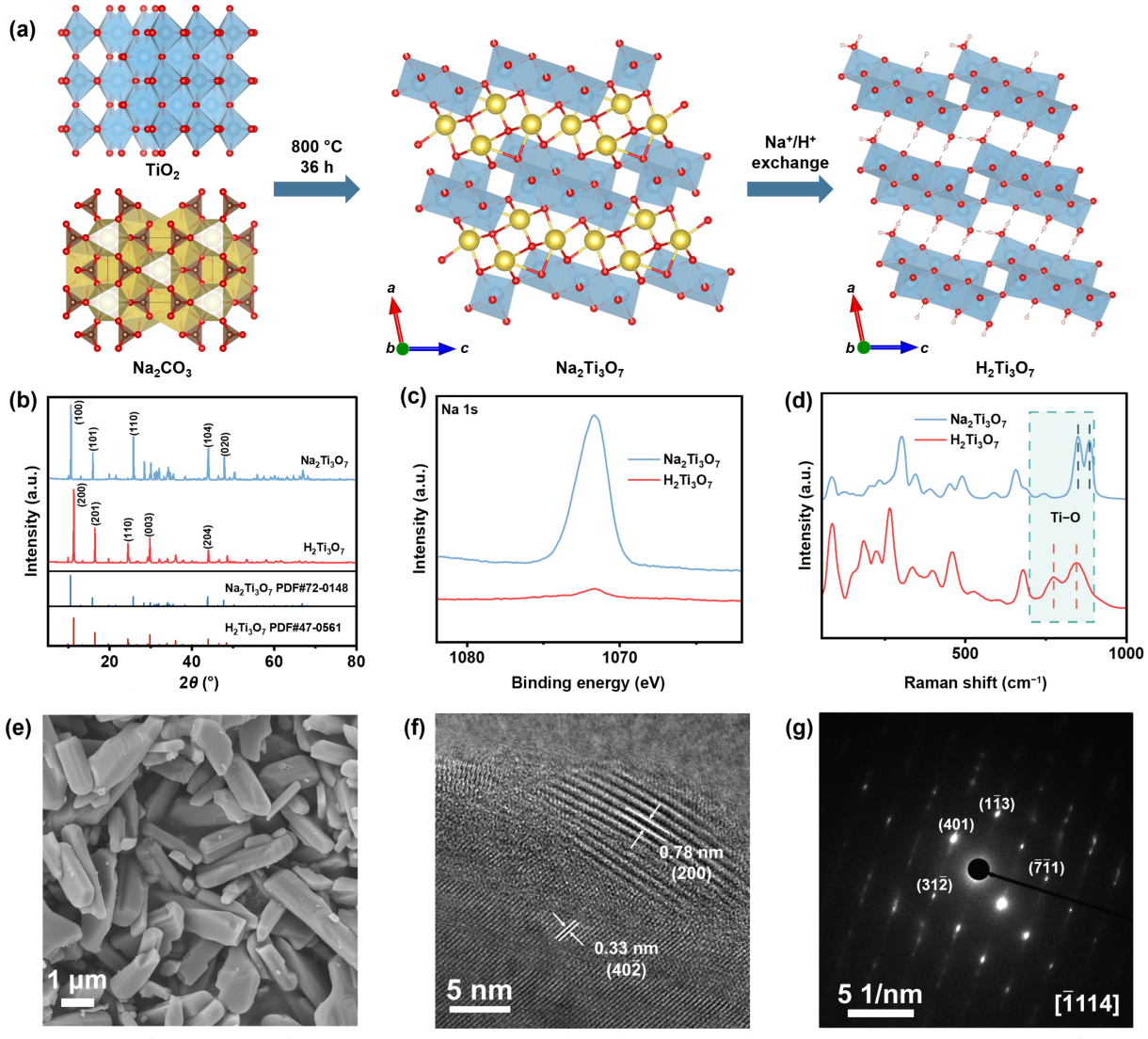

Figure 1 (a) Illustration of the preparation of HTO. Blue balls: Ti; red balls: O; yellow balls: Na; brown balls: C; and pink balls: H. (b) XRD patterns of HTO and NTO materials. (c) The high-resolution XPS spectra of Na 1s. (d) Raman spectra of NTO and HTO materials. (e) SEM image, (f) HRTEM image, and (g) SAED pattern of the HTO material.

(GF-A) as the membrane, and 3 mol·kg^{-1} zinc trifluoromethanesulfonate ($Zn(OTf)_2$) as the electrolyte. First, the influence of different electrolytes on the HTO electrode was systematically investigated, as summarized in Fig. S7 in the ESM. The HTO electrode shows poor performance in 1 m zinc acetate ($Zn(Ac)_2$) electrolyte, with an ultra-low Coulombic efficiency of 50%. In 1 m $ZnSO_4$ electrolyte, the working potentials of HTO were the highest among all electrolytes, exceeding those in $Zn(OTf)_2$-based systems. However, although 1 m $ZnSO_4$ provided the highest working potential, its Coulombic efficiency remained lower than that of $Zn(OTf)_2$ electrolytes, suggesting more severe side reactions in $ZnSO_4$. Considering the relatively low reaction potential and the highest Coulombic efficiency, 3 m $Zn(OTf)_2$ was selected as the most suitable electrolyte for subsequent experiments.

Figure 2(a) shows the cyclic voltammetry (CV) curves of HTO and NTO electrodes with the potential range from −0.03 to 1.6 V vs. Zn^{2+}/Zn at the scan rate of 0.2 mV·s^{-1}. A pair of distinct redox peaks is observed in the CV curves of HTO electrode, located at 0.05 and −0.02 V vs. Zn^{2+}/Zn during the oxidation and reduction process, respectively. The nearly overlapping curves of the first three cycles indicate the highly reversible electrochemical behavior of the HTO electrode in AZIBs. In contrast, the CV curves of the NTO electrode exhibit no discernible redox peaks, suggesting its limited electrochemical activity in AZIBs. The kinetics of the HTO electrode during the electrochemical process were further investigated through CV profiles at various scan rates from 0.1 to 0.4 mV·s^{-1}, as shown in Fig. S8 in the ESM. The relationship of the peak current (i) and the scan rate (v) was analyzed using the empirical power-law equation $i = av^b$, where a and b are coefficients. The b value serves as a quantitative indicator of the charge storage mechanism. A b value of 0.5 is typically associated with a diffusion-controlled process, while a b value of 1.0 indicates a capacitive process. As shown in Fig. 2(b), the b values of the oxidation peak (Peak 1) and reduction peak (Peak 2) are 0.496 and 0.508, respectively, suggesting both the insertion and extraction of Zn^{2+} are predominantly governed by diffusion-controlled mechanisms.

Figure 2(c) and Fig. S9 in the ESM display the galvanostatic charge–discharge (GCD) profiles of the HTO and NTO electrodes at the current density of 0.2 A·g^{-1}, within a voltage range window

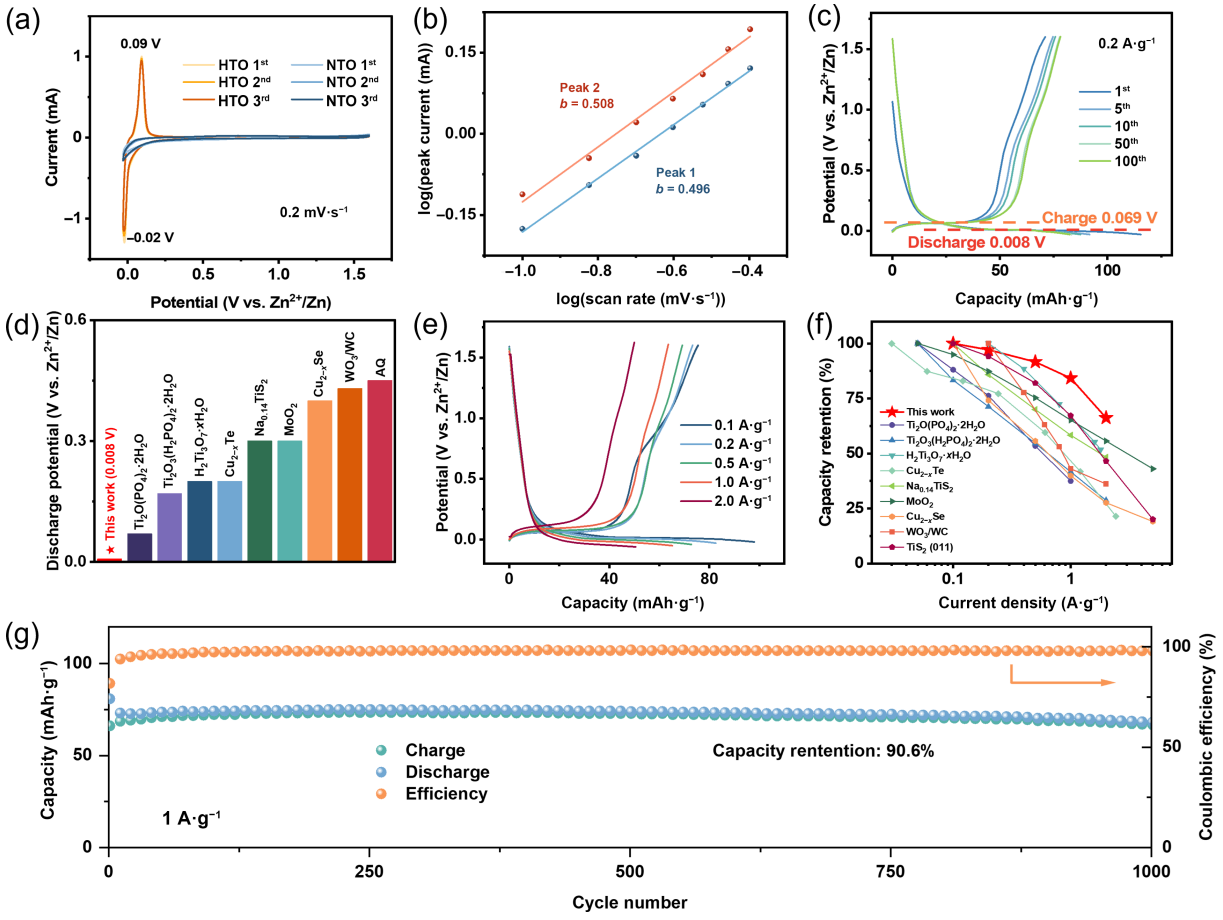

Figure 2 (a) CV curves of HTO and NTO electrodes at the scan rate of 0.2 mV·s^{-1}. (b) Relationship between peak current and scan rate. (c) GCD profiles of the HTO electrode at 0.2 A·g^{-1}. (d) Comparison of the average discharge potential among the reported intercalated AZIBs anodes [16, 18, 20–22, 32–35]. (e) Rate performance of the HTO electrode. (f) Comparison of the rate performances between the HTO electrode and reported intercalated AZIBs anodes [15, 16, 18, 20–22, 32–34]. (g) Cycling performance of the HTO electrode at 1 A·g^{-1}.

ranging from −0.03 to 1.6 V vs. Zn^{2+}/Zn, respectively. Notably, even at a discharge cutoff voltage below 0 V vs. Zn^{2+}/Zn, metallic zinc deposition remains inhibited due to the kinetic deposition overpotential until the potential reaches −0.05 V vs. Zn^{2+}/Zn, as presented in Fig. S10 in the ESM. In addition, the impact of temperature fluctuations on the safety discharge margin of the HTO||Zn cell was further evaluated. As shown in Fig. S11 in the ESM, the discharge plateau potential of HTO is −0.006, 0.008, and 0.01 V at temperatures of 10, 30, and 50 °C, respectively. Meanwhile, the Zn deposition potentials are −0.062, −0.046, and −0.031 V at temperatures of 10, 30, and 50 °C, respectively. Both the discharge plateau potential of the HTO electrode and the Zn deposition potential increase as the temperature rises, indicating that there is enough safe margin for the HTO electrode to fully release its capacity regardless of the temperature.

The HTO electrode delivers an initial discharge and charge capacity of 115.48 and 71.03 mAh·g^{-1}, respectively, corresponding to an initial Coulombic efficiency (ICE) of 61.5%. After 100 cycles, a reversible capacity of 78.09 mAh·g^{-1} is retained, highlighting the excellent cycling stability of the HTO electrode. In addition, even with a higher active mass loading of 12.8 mg·cm^{-2}, the HTO cell can still work normally, demonstrating its potential for practical applications (Fig. S12 in the ESM). In contrast, the NTO electrode exhibits negligible electrochemical activity with a significantly lower capacity of approximately 20 mAh·g^{-1}, which aligns with the CV results. Even when the discharge cutoff is set at −0.1 V vs. Zn^{2+}/Zn, the NTO electrode still shows limited capacity (Fig. S9(b) in the ESM). This discrepancy further demonstrates that the Na^+/H^+ ion exchange process plays a crucial role in enhancing the electrochemical activity of the material in AZIBs.

The work function (Φ) of both NTO and HTO through ultraviolet photoelectron spectroscopy (UPS) with −5 V bias was measured to further elucidate the poor redox activity of the NTO electrode, as displayed in Fig. S13 in the ESM. Argon ion sputtering was used before sample testing to avoid interference from surface contamination. The work functions for NTO and HTO are 2.62 and 3.04 eV, respectively. Since there exists an approximate linear relationship between the working potential of electrode material and its work function, as discussed in the ESM, the lower work function of NTO implies its lower redox potential, which may be lower than the deposition potential of zinc or the hydrogen evolution potential of water. As a result, NTO electrode exhibits poor redox activity in aqueous Zn-ion batteries.

Impressively, both charge and discharge plateaus emerge below 0.1 V vs. Zn^{2+}/Zn in HTO, with the average charge and discharge voltages of the HTO electrode of 0.069 and 0.008 V vs. Zn^{2+}/Zn, respectively (Fig. 2(c)), which align well with the ultra-low redox peaks in CV profiles presented in Fig. 2(a). To eliminate the interference caused by the overpotential of the Zn anode on the potential measurement of the HTO cathode in the coin-cell system,

GCD curves were collected using a three-electrode configuration, with the HTO electrode as the working electrode, a Zn foil as the counter electrode, and another Zn foil as the reference electrode. As shown in Fig. S14 in the ESM, more accurate redox plateaus were observed in the three-electrode system, with voltages of 0.012 V during discharge and 0.055 V during charge. Compared to the results obtained in the coin-cell system, the polarization is further reduced, as evidenced by the decrease in the voltage gap between the charging and discharging plateaus from 0.06 to 0.04 V, indicating the superior electrochemical kinetics of the HTO electrode.

Figure 2(d) and Table S4 in the ESM further compare the discharge potentials of the HTO electrode with those of other reported intercalated anodes for AZIBs [16, 18, 20–22, 32–35]. The HTO electrode exhibits the lowest Zn^{2+} intercalation potential among all reported "rocking-chair" intercalated anodes for AZIBs to the best of our knowledge, making it a highly promising candidate as the anode for high-voltage and high-energy-efficiency aqueous batteries. Notably, in comparison with previously reported nano-sized $H_2Ti_3O_7$-based anodes for AZIBs, such as $H_2Ti_3O_7{\cdot}xH_2O$ [20] and MXene/titanic acid [19], micro-sized HTO in this work delivers a significantly lower working potential. This difference is attributed to several reasons, including variations in morphology, distinct reaction mechanisms (solid solution reaction/two-phase reaction mechanism), and differences in electrolyte usage. A detailed discussion on the effect of morphology on the electrochemical plateau is provided in Supplementary Notes S1 and S2 in the ESM.

The rate performance of the HTO electrode was also evaluated, as depicted in Fig. 2(e). The reversible capacities are 75.52, 73.33, 69.21, 63.61, and 50.00 $mAh{\cdot}g^{-1}$ at current densities of 0.1, 0.2, 0.5, 1.0, and 2.0 $A{\cdot}g^{-1}$, respectively. Notably, even at a high current density of 2.0 $A{\cdot}g^{-1}$, the HTO electrode retains 66% of its capacity compared to that at 0.1 $A{\cdot}g^{-1}$, while maintaining its low redox plateaus. Such excellent rate capability demonstrates superior kinetics, which surpasses many previously reported results (Fig. 2(f) and Table S4 in the ESM) [15, 16, 18, 20–22, 32–34]. Figure 2(g) illustrates the long-term cycling performance of the HTO electrode at a current density of 1 $A{\cdot}g^{-1}$. The HTO electrode maintains an exceptional lifespan exceeding 1000 cycles with 90.6% capacity retention, demonstrating its great potential as an anode for long-life AZIBs.

Considering polarization at high current densities may trigger metallic zinc plating, XRD, XPS, and SEM measurements were applied to the HTO electrode after 300 cycles at 1 $A{\cdot}g^{-1}$ to further exclude the possibility of metallic zinc deposition. Figure S15(a) in the ESM displays the XRD pattern of the HTO electrode after 300 cycles at 1 $A{\cdot}g^{-1}$. The main peaks can be assigned to basic zinc salt (BZS, $Zn_{12}(CF_3SO_3)_9(OH)_{15}{\cdot}nH_2O$), HTO, polytetrafluoroethylene (PTFE) binder, and Ti current collector. No peak corresponding to Zn metal (PDF#65-5973) can be observed in the XRD result, indicating the absence of zinc plating. The high-resolution XPS spectra of Zn 2p are shown in Fig. S15(b) in the ESM. A shift of both Zn $2p_{3/2}$ and Zn $2p_{1/2}$ in the HTO electrode can be observed when compared with the peaks in the Zn metal foil. To further exclude the possibility of metallic zinc deposition, Zn LMM Auger spectra were also evaluated, as shown in Fig. S15(c) in the ESM. No peak corresponding to Zn metal (993.0 and 996.4 eV, highlighted in the red box) can be observed in HTO electrode after cycling, confirming the non-existence of metal Zn on the surface of HTO electrode. SEM image with corresponding EDS mapping images in Fig. S15(d) in the ESM shows that there are micro rods and flakes distributed on the surface of the electrode after cycling, corresponding to HTO material and BZS, respectively. In summary, XRD, XPS, and SEM measurements prove that zinc would not deposit on the surface of the HTO electrode even under high current density and long-term cycling.

2.3 Zn^{2+} storage mechanism

The reaction mechanism of the HTO electrode was systematically investigated through *in situ* XRD, ICP-OES, XPS, and EDS measurements. The reaction mechanism of the HTO electrode was systematically investigated through *in situ* XRD, ICP-OES, XPS, and EDS measurements. *In situ* XRD patterns collected during the first three galvanostatic cycling (Fig. 3) reveal a hybrid reaction mechanism. At initial discharge, the voltage drops rapidly until the potential reaches the platform of approximately 0.005 V vs. Zn^{2+}/Zn, with only slight changes observed in the *in situ* XRD patterns that (003) and $(60\bar{2})$ planes shift to lower angles, indicating the single-phase reaction. The subtle angular changes suggest minimal lattice expansion during the ion insertion process, thereby enhancing the structural stability of the material during the electrochemical process. Afterward, the GCD curves exhibit a flat plateau, indicating a typical two-phase reaction, accompanied by the disappearance of existing peaks and the emergence of new peaks. Specifically, characteristic peaks located at 11.09°, 16.30°, 24.27°, 24.61°, 26.35°, 29.57°, 31.90°, 33.94°, and 35.67°, which correspond to (200), (201), (110), (202), (401), (003), (311), (203), and $(60\bar{2})$ planes, respectively, disappear when the potential drops below 0.005 V vs. Zn^{2+}/Zn during the discharge process. At the same time, new peaks emerge at 11.57°, 16.89°, 25.19°, 26.23°, 29.63°, 32.92°, 34.59°, and 36.32°, which indicates the formation of a new phase (partially highlighted with purple boxes in Fig. 3(b)). These new peaks disappear upon charging, confirming the high reversibility of the transformation. The overall reaction mechanism involves the single-phase reaction and the two-phase reaction, as illustrated in Fig. 4(a). This mechanism is different from the previously reported nano-sized $H_2Ti_3O_7{\cdot}xH_2O$ [20] and MXene/titanic acid [19], in which only a solid solution reaction was observed during the Zn^{2+} (de)intercalation process. This difference in reaction mechanisms may result from the different morphology, as discussed in Supplementary Note S2 in the ESM.

Besides, it is worth noting that two distinct diffraction peaks located at 6.45° and 12.97° (highlighted with green boxes) emerge during discharge process and vanish during charge process, which can be attributed to the reversible BZS. This reversible interfacial product serves as an indicator of the reversible (de)insertion of H^+ in aqueous batteries, as supported by previous studies [21, 36–38]. In addition, the *in situ* XRD patterns exhibit nearly identical changes across the first three cycles, indicating their excellent reversibility during the electrochemical process.

The (de)insertion of Zn^{2+} was further confirmed by ICP measurements, as shown in Fig. 4(b). The atomic ratio of Zn/Ti was analyzed at four distinct states of charge (SOC), as shown in Fig. 4(a). The measured values were 0.037, 0.076, 0.059, and 0.014 for Points A, B, C, and D, respectively. The huge difference in the Zn/Ti atomic ratio at different SOCs demonstrates the Zn^{2+} insertion/extraction during the electrochemical process. The small amount of Zn detected after the first charge (Point D) suggests the presence of residual Zn^{2+} within the HTO structure, which aligns with the low ICE observed in the GCD profile.

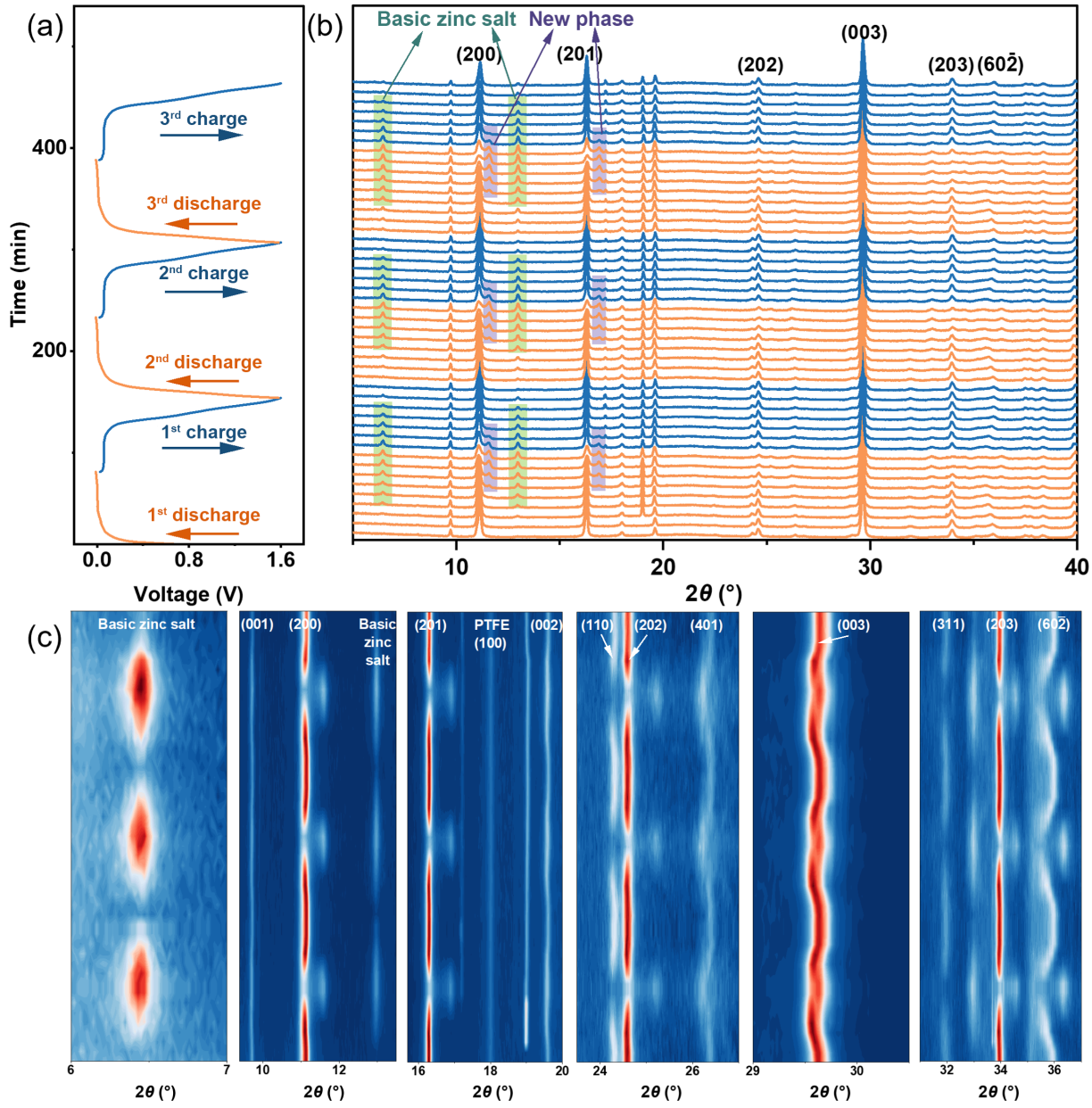

Figure 3 (a) GCD profiles for the *in situ* XRD measurement. (b) *In situ* XRD patterns and (c) enlarged areas of the *in situ* XRD patterns.

SEM and corresponding EDS tests at different SOCs were also conducted. The nanorod morphology of the HTO remains unchanged throughout the electrochemical process, as illustrated in Fig. S16 in the ESM, demonstrating the excellent structural stability of HTO in AZIBs. EDS mapping of the HTO electrode at the discharged state (Point B) in Fig. 4(c) reveals a distinct aggregation of the Zn and F elements, as highlighted in the yellow circle, which can be attributed to the formation of the reversible BZS that generates along with the incorporation of H^+. Upon charging (Point D), the aggregation of the Zn and F elements disappears (Fig. S17 in the ESM), suggesting the reversible extraction of H^+ from the HTO electrode, which is consistent with the *in situ* XRD results in Fig. 3. From Fig. 4(c) and Fig. S15(d) in the ESM, a separation of the HTO rods and the flaky BZS by-product can be discerned at the discharged state. O and Ti elements are concentrated on the HTO rods, while F and Zn elements are concentrated on the surrounding flaky by-products, indicating the potential to reduce the interference of surface BZS by-products on measuring the contribution of the intercalated Zn at high magnification, where the EDS measurement focuses on the smooth surface of the HTO rods. Figure S18 in the ESM exhibits the results of EDS measurements of the HTO electrode at different SOCs with the magnification of 50,000× and 1000×, respectively. The detailed data are displayed in Figs. S19–S22 in the ESM. Two different positions were selected at 50,000× in order to improve the reliability of the results. At a high magnification of 50,000×, only signals within a few hundred nanometers of the HTO rod are collected (in the white box), where the Zn signal primarily originates from the Zn^{2+} intercalated in the structure of HTO. While at a low magnification of 1000×, the collected signal is jointly contributed by HTO and by-products. As shown in Fig. S18 in the ESM, both Zn and S element ratios decrease at 50,000× compared to 1000×, with the S atomic ratio remaining below 1% in all samples at 50,000×, indicating the reduced interference of BZS by-products at a high magnification.

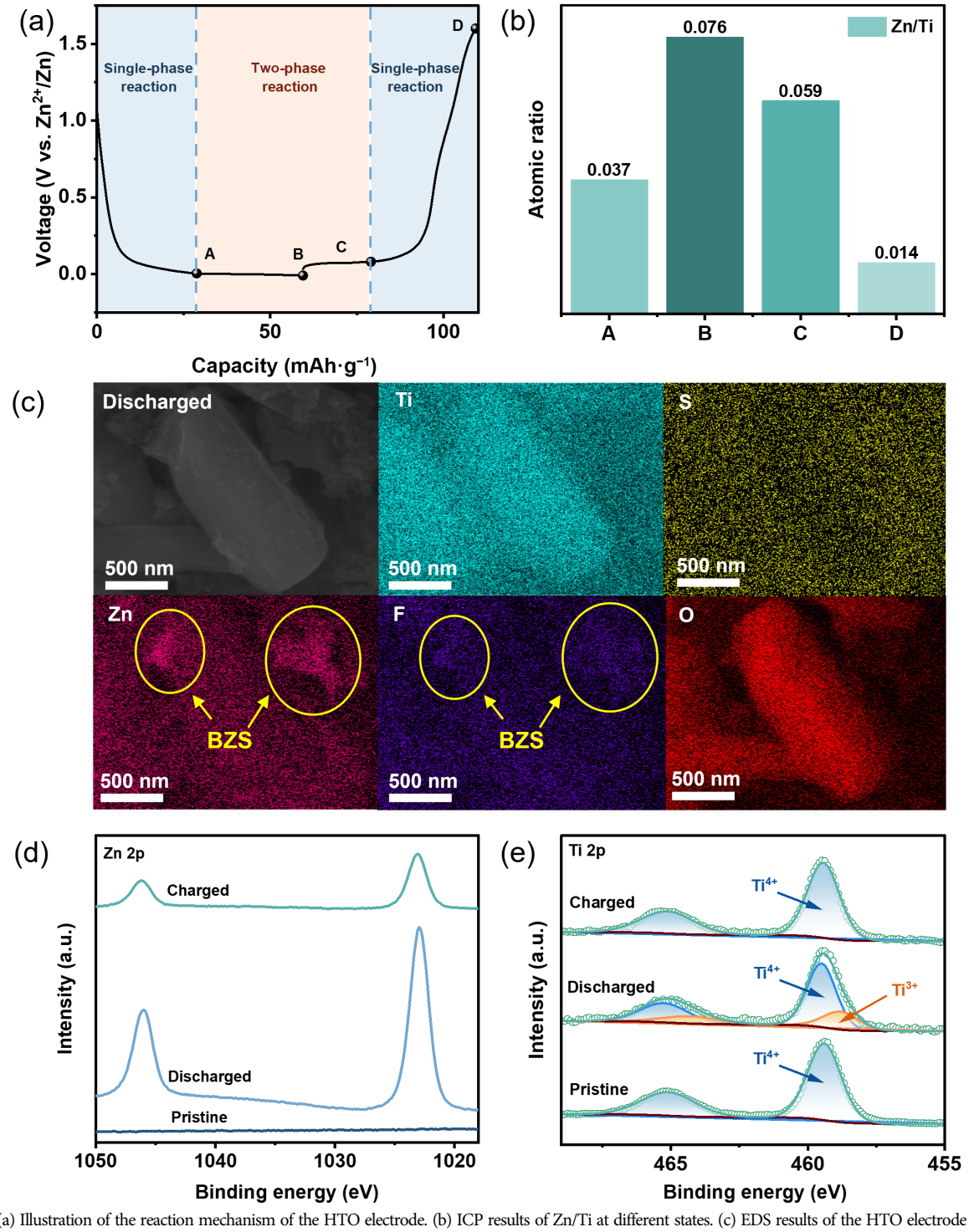

Figure 4 (a) Illustration of the reaction mechanism of the HTO electrode. (b) ICP results of Zn/Ti at different states. (c) EDS results of the HTO electrode at first fully discharged state. High-resolution XPS spectra of the HTO electrode at different states: (d) Zn 2p and (e) Ti 2p.

The Zn ratio in 50,000× increases in the discharge process (pristine → A and A → B), and decreases in the charge process (B → C and C → D), demonstrating the reversible (de)intercalation of Zn^{2+} in HTO.

The H^+ contribution was further measured through pH monitoring and comparative electrolyte experiments. An H-cell was employed for pH monitoring, with the pH electrode and HTO cathode on one side and Zn metal anode on the other side, to eliminate the influence of Zn corrosion and hydrogen evolution on pH value (Fig. S23(a) in the ESM). The pH electrode and HTO electrode were placed as close as possible. Throughout the entire charging and discharging process, the pH value only exhibits a slight increase, which might be attributed to the temperature rise from 22.8 to 23.5 °C caused by the charging and discharging process (Fig. S23(b) in the ESM).

In addition, comparative experiments using H_2SO_4 electrolyte and anhydrous organic electrolyte were carried out to explore the proton contribution. To investigate H^+ intercalation, a Ti electrode,

an Ag/AgCl electrode, and H_2SO_4 electrolyte (pH = 3) were employed as the counter electrode, reference electrode, and electrolyte, respectively, to eliminate the influence of Zn^{2+}. As depicted in Fig. S23(c) in the ESM, severe hydrogen evolution is observed in the discharge curve, and only a limited reversible capacity (approximately 5 mAh·g^{-1}) can be detected during the charging process. The minimal fluctuation in pH value and the restricted reversible capacity in H_2SO_4 electrolyte jointly demonstrate the less contribution of H^+ compared to Zn^{2+} in the (co)intercalation process.

Moreover, XPS measurements were conducted to analyze the chemical states of the HTO electrode at various SOCs. The XPS survey spectra of the HTO electrodes are presented in Fig. S24 in the ESM. The Ti and O peaks originate from the HTO material, whereas the F and C peaks are attributed to the PTFE binder and Ketjen black conductive agent, respectively. The detection of Zn peaks suggests the occurrence of electrochemical intercalation of Zn^{2+}, a phenomenon that is more distinctly discernible in the high-resolution Zn 2p spectra presented in Fig. 4(d). In the pristine state, no signal of Zn 2p can be detected. After discharge, a set of sharp peaks corresponding to Zn 2p emerges, which can be attributed to the insertion of Zn^{2+} into the HTO lattice structure as well as the formation of interfacial by-products. Upon completion of charging, the Zn 2p signal weakens significantly, indicating the deintercalation of Zn^{2+} from the electrode. The high-resolution Ti 2p spectra are presented in Fig. 4(e). Both the pristine and fully charged HTO electrodes showcase a set of doublet peaks around 465.2 and 459.5 eV, which correspond to the $2p_{1/2}$ and $2p_{3/2}$ orbitals of Ti^{4+}, respectively. Upon discharge, an extra set of peaks becomes apparent near the binding energy of approximately 458.8 eV, suggesting the reduction of Ti^{4+} to Ti^{3+} resulting from the intercalation of Zn^{2+}/H^+.

2.4 Electrochemical performance of rocking-chair KZnHCF||HTO battery

To further investigate the electrochemical performance of the HTO anode, a "rocking-chair" type full AZIB was fabricated, with KZnHCF as the cathode, HTO as the anode, and 3 mol·kg^{-1} $Zn(OTf)_2$ as the electrolyte, as illustrated in Fig. 5(a). KZnHCF was chosen as the cathode due to its robust framework, large ion channels, and high redox plateaus (1.8 V vs. Zn^{2+}/Zn, Fig. 5(b)). The detailed information of the KZnHCF cathode is shown in Fig. S25 in the ESM. To better reflect practical application conditions, the capacity ratio of the positive electrode to the negative electrode (P/N ratio) in the full cell was set close to 1, with a high active mass loading of 9.96 mg·cm^{-2} for KZnHCF cathode and 6.11 mg·cm^{-2} for HTO anode.

As shown in Fig. 5(c) and Fig. S26 in the ESM, the KZnHCF||HTO full battery delivers a reversible capacity of 62 mAh·g^{-1} at 0.2 A·g^{-1} (calculated based on the mass of HTO),

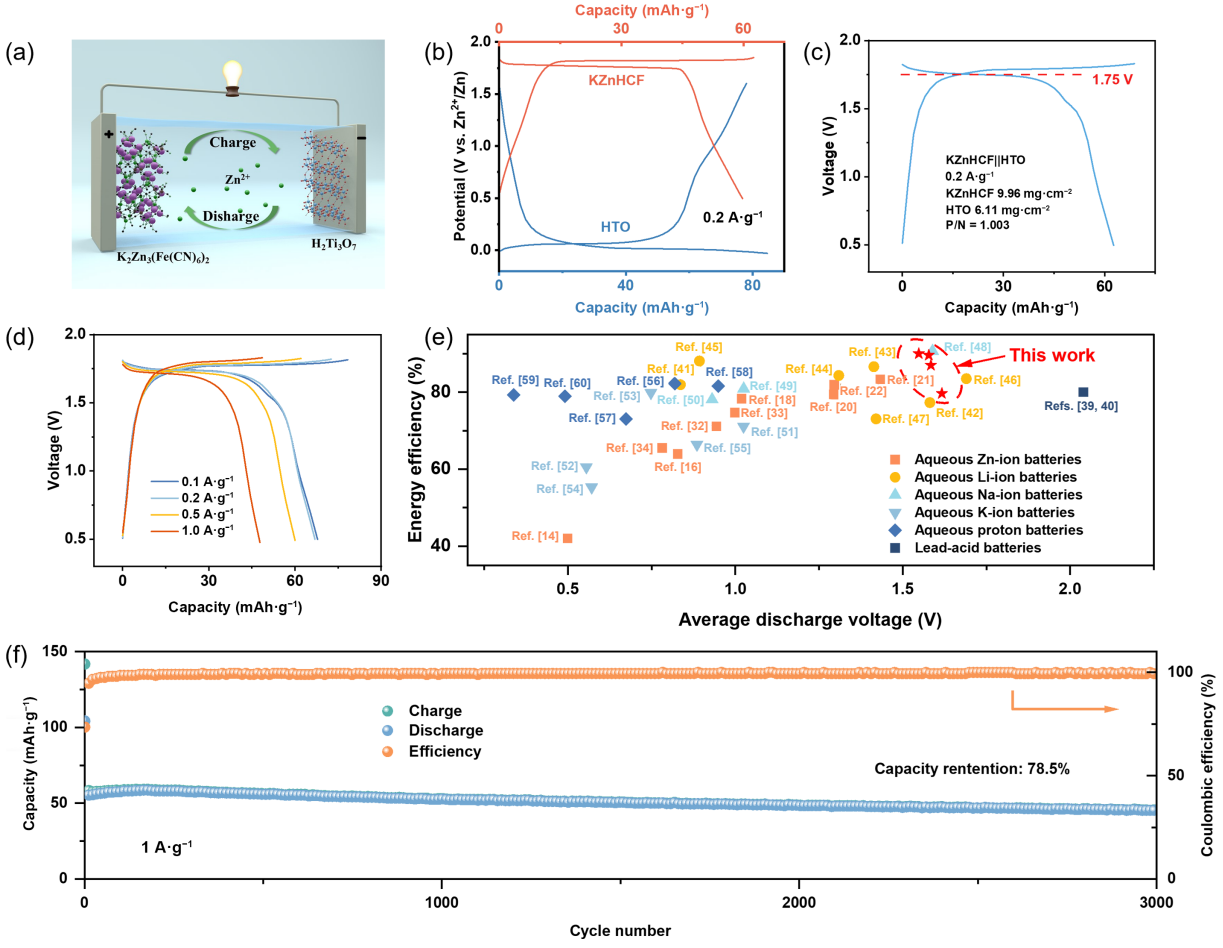

Figure 5 (a) Scheme of the KZnHCF||HTO full battery. (b) GCD profiles of the KZnHCF cathode and the HTO anode at the current density of 0.2 A·g^{-1}. (c) GCD profiles of the KZnHCF||HTO full battery at 0.2 A·g^{-1}. (d) Rate performance of the KZnHCF||HTO full battery. (e) Comparison of voltage and energy efficiency with other batteries [14, 16, 18, 20–22, 32–34, 39–60]. (f) Long-term cycle performance of the KZnHCF||HTO full battery.

along with a high Coulombic efficiency of 97%. Owing to the low redox potential of the HTO anode, the KZnHCF||HTO full battery displays a high discharge plateau of 1.75 V (Fig. 5(c)). Figure 5(d) and Fig. S27 in the ESM show the rate performance of the KZnHCF||HTO battery, delivering capacities of 67.8, 66.9, 60.0, and 47.8 mAh·g^{-1} at current densities of 0.1, 0.2, 0.5, and 1.0 A·g^{-1}, respectively.

In addition, the KZnHCF||HTO full battery demonstrates a notable advantage in terms of EE compared to previously reported "rocking-chair" AZIBs, exhibiting EE of 79.7%, 87.0%, 89.6%, and 90.0% at current densities of 0.1, 0.2, 0.5, and 1.0 A·g^{-1}, respectively (Table S5 in the ESM). Energy efficiency, although often overlooked in aqueous battery research, is a critical factor for practical applications. The KZnHCF||HTO battery achieves an impressive energy efficiency of 90%, which is the highest among the reported "rocking-chair" AZIBs to our best knowledge and even rivals commercial lead-acid batteries (EE = 70%–80%) [39, 40]. The average discharge voltage and the EE between KZnHCF||HTO in this work are compared with other aqueous rocking-chair type batteries, including Zn-ion batteries [14, 16, 18, 20–22, 32–34], Li-ion batteries [41–47], Na-ion batteries [48–50], K-ion batteries [51–55], and proton batteries [56–60], as displayed in Fig. 5(e) and Table S5 in the ESM. In this comparison figure, average discharge voltage is used instead of the plateau voltage, because some of the batteries do not have a flat discharge plateau (discussed in Supplementary Note S3 in the ESM). The combination of high output voltage and high energy efficiency endows this battery with significant potential for practical applications in energy storage systems. It is worth noting that although some Li-ion and Na-ion batteries exhibit higher voltage or energy efficiency, they utilize the "water-in-salt" electrolyte to expand the electrochemical stability window, including 21 m lithium bis(trifluoromethanesulfonyl) imide (LiTFSI) electrolyte [42], 12.5 m $LiNO_3$ localized water-in-salt gel electrolyte [46], and 19 m $NaClO_4$-NaOTf-H_2O electrolyte [48]. The usage of the "water-in-salt" electrolyte increases the cost and viscosity of the electrolyte, thereby restricting its practical application. In contrast, the KZnHCF||HTO cell in this work achieves comparable discharge voltage and energy efficiency with the conventional 3 m $Zn(OTf)_2$ electrolyte to those batteries employing "water-in-salt" electrolyte, further demonstrating the superiority of the HTO anode.

Furthermore, the cycle stability of the KZnHCF||HTO full cell was evaluated. In the cycling test, the stability of the full cell is dominated by the rapid degradation of KZnHCF cathode under low P/N ratio (Figs. S28 and S29 in the ESM). To make HTO anode fully release its capacity and cycling stability, an excessive KZnHCF cathode was used with the P/N ratio of 6.5 in the long cycle test. The KZnHCF||HTO cell demonstrates excellent cycle stability, retaining 78.5% of its initial capacity after 3000 cycles at a current density of 1 A·g^{-1} (Fig. 5(f)).

To further highlight the advantage of HTO as a metal-free anode in terms of energy density, three common cathodes, including MnO_2 (308 mAh·g^{-1}, 1.3 V), V_2O_5 (400 mAh·g^{-1}, 0.8 V), and $K_2Mn[Fe(CN)_6]$ (100 mAh·g^{-1}, 1.7 V) [61], were selected to calculate the theoretical energy densities of the full cells at an N/P ratio of 1. As displayed in Table S6 and Fig. S30 in the ESM, the MnO_2||HTO, V_2O_5||HTO, and $K_2Mn[Fe(CN)_6]$||HTO full batteries deliver energy densities of 76.6, 47.7, and 71.5 Wh·kg^{-1}, respectively. These values exceed those of corresponding Zn-metal-based batteries with 5% Zn utilization and are substantially higher than the energy density of lead-acid batteries (30 Wh·kg^{-1}) [62]. Only when the utilization rate of the Zn anode reaches 10% is the energy density of the Zn metal-based battery comparable to that of the HTO "rocking-chair" battery. Considering that the utilization in most reported AZIBs is below 5% [21], the HTO anode exhibits significant advantages in energy density relative to conventional zinc metal anodes.

In summary, the high output voltage, high energy density, and the excellent cycle performance of KZnHCF||HTO highlight its potential as a promising candidate for next-generation aqueous batteries, demonstrating the distinct superiorities of HTO with ultra-low potential over other metal-free intercalative anodes for "rocking-chair" AZIBs.

3 Conclusions

In summary, $H_2Ti_3O_7$ with an ultra-low redox potential of 0.008 V vs. Zn^{2+}/Zn was developed through Na^+/H^+ ion exchange from $Na_2Ti_3O_7$. This material effectively addresses the critical limitations of conventional Zn metal anodes and outperforms existing intercalative anodes plagued by high redox potentials. The HTO anode delivers remarkable cycling stability (90.6% retention after 1000 cycles) and superior high-rate capability. *In situ* XRD analysis elucidates a two-phase transformation reaction mechanism during Zn^{2+} (de)intercalation, distinct from the solid–solution behavior observed in other hydrated titanic acid anodes. Furthermore, a 1.75 V rocking-chair full cell with a high energy efficiency of 87% at 0.2 A·g^{-1} is realized by coupling the HTO anode with the KZnHCF cathode. The full cell exhibits impressive cycling stability, retaining 78.5% of its initial capacity after 3000 cycles. This work offers a promising strategy to address the critical challenges associated with metallic Zn anodes through developing intercalative anodes with low redox potential, thereby facilitating the progress toward practical AZIBs.

4 Experimental methods

4.1 Material synthesis

4.1.1 *Synthesis of $Na_2Ti_3O_7$*

15 mmol titanium dioxide (Aladdin, analytical reagent (AR)) and 5.25 mmol sodium carbonate (Aladdin, AR) were ground for 30 min with a small amount of ethanol. The mixture was then heated at 800 °C for 36 h in air, with intermittent grinding every 12 h [23].

4.1.2 *Synthesis of $H_2Ti_3O_7$*

HTO was synthesized from NTO via a Na^+/H^+ ion exchange process conducted in hydrochloric acid solution, as previously reported [24]. Specifically, 1 g of NTO powder was added into 100 mL of 1 mol·L^{-1} HCl solution and stirred continuously for 48 h. After the acidic treatment, the resulting HTO was washed thoroughly with deionized water and then dried overnight at 80 °C in air.

4.1.3 *Synthesis of KZnHCF*

15 mmol potassium citrate (Aladdin, ≥ 98%) was added into 100 mL of 0.01 mol·L^{-1} $ZnSO_4$ (Aladdin, AR) solution and stirred for 30 min. Subsequently, 100 mL of 0.01 mol·L^{-1} $K_4Fe(CN)_6{\cdot}3H_2O$ (Aladdin, AR, ≥ 99%) solution was added to the above solution and stirred for 24 h. The resulting product was then filtered, washed

with deionized water, and dried overnight at 110 °C in a vacuum oven.

4.2 Material characterization

XRD experiment was performed on a Bruker D8 Discover diffractometer with Cu Kα (λ = 1.5406 Å). Morphology information was collected with TEM (JEOL JEM-F200) and SEM (ZEISS SUPRA®55) with an energy dispersive spectrometer (EDS) for elemental analysis. Raman spectra were collected using WITec alpha300R with laser excitation at 532 nm. The element composition was analyzed using XPS (Thermo Scientific K-Alpha). TGA was conducted with TA Discovery TGA 550. ICP-OES was conducted with Agilent 5110(OES). Work function was measured through UPS (Thermo Fisher Scientific ESCALAB Xi) with −5 V bias.

4.3 Electrochemical measurements

The active materials, Ketjen black (Canrd, ECP-600JD) and PTFE (Aladdin, 60 wt.%), were mixed with a weight ratio of 7:2:1 with the diluent of isopropyl alcohol (Aladdin, AR, ≥ 99.7%). The mixture was pressed and cut into disks (with a diameter of 7 mm). After drying in a vacuum oven at 60 °C overnight, the disk was pressed into a Ti mesh. The average mass loading of active material was ~ 4.2 mg·cm^{-2}. The electrochemical properties of HTO||Zn cells were performed using CR2032 coin cells that were assembled with Ti mesh as the current collector, glass fiber (GF-A) as the separator, Zn foil (Canrd, 99.99%, 200 μm) as the anode, and 3 mol·kg^{-1} $Zn(CF_3SO_3)_2$ ($Zn(OTf)_2$, Aladdin, ≥ 98%) aqueous solution as the electrolyte. The electrochemical properties of KZnHCF||HTO full cells were performed using CR2032 coin cells that were assembled with Ti mesh as the current collector, glass fiber (GF-A) as the separator, HTO as the anode, KZnHCF as the cathode, and 3 mol·kg^{-1} $Zn(CF_3SO_3)_2$ ($Zn(OTf)_2$, Aladdin, ≥ 98%) aqueous solution as the electrolyte, with the P/N close to 1. The average mass loading of active material was ~ 10 mg·cm^{-2} for KZnHCF cathode and that was ~ 6 mg·cm^{-2} for HTO anode. The GCD measurements were performed on a Neware battery testing system. For the half-cell, the charge voltage was limited to 1.6 V, while the discharge cutoff potentials were set to be −0.02, −0.03, −0.04, −0.05, and −0.06 V for current densities of 0.1, 0.2, 0.5, 1.0, and 2.0 A·g^{-1}, respectively. In the case of the full-cell, the discharge voltage was limited to 0.5 V, and the charge cutoff voltages were set at 1.815, 1.82, 1.825, and 1.83 V for current densities of 0.1, 0.2, 0.5, and 1.0 A·g^{-1}, respectively. The CV tests were conducted on an Admiral Squidstat Plus electrochemical workstation. The energy efficiencies of reported batteries were estimated based on their GCD curves, which were extracted using WebPlotDigitizer.

Electronic Supplementary Material: Supplementary material (XPS, TGA, SEM, EDS, other electrochemical test results, and Supplementary Notes S1–S3) is available in the online version of this article at https://doi.org/10.26599/NR.2026.94908435.

Data availability

All data needed to support the conclusions in the paper are presented in the manuscript and the Electronic Supplementary Material. Additional data related to this paper may be requested from the corresponding author upon request.

Acknowledgements

This work was supported by the Key-Area Research and Development Program of Guangdong Province (No. 2023B0909010001), Shenzhen Polytechnic University Research Fund (No. 6025310001K), and the National Natural Science Foundation of China (No. 22575156).

Declaration of competing interest

All the contributing authors report no conflict of interests in this work.

Author contribution statement

X. Y. G.: Formal analysis, investigation, methodology, validation, visualization, writing – original draft. Y. C.: Validation. Y. Z.: Visualization. J. K. L.: Validation. P. H.: Validation. Y. T.: Validation. W. J. D.: Funding acquisition, investigation, resources, validation, writing – review & editing. R. L.: Conceptualization, funding acquisition, resources, supervision, writing – review & editing. All the authors have approved the final manuscript.

Use of AI statement

None.

References

[1] Zhu, J. C.; Tie, Z. W.; Bi, S. S.; Niu, Z. Q. Towards more sustainable aqueous zinc-ion batteries. *Angew. Chem., Int. Ed.* **2024**, *63*, e202403712.

[2] Hao, J. N.; Zhang, S. J.; Wu, H.; Yuan, L. B.; Davey, K.; Qiao, S. Z. Advanced cathodes for aqueous Zn batteries beyond Zn^{2+} intercalation. *Chem. Soc. Rev.* **2024**, *53*, 4312–4332.

[3] Dong, D. J.; Wang, T. R.; Sun, Y.; Fan, J.; Lu, Y. C. Hydrotropic solubilization of zinc acetates for sustainable aqueous battery electrolytes. *Nat. Sustain.* **2023**, *6*, 1474–1484.

[4] Tian, H. J.; Feng, G. X.; Wang, Q.; Li, Z.; Zhang, W.; Lucero, M.; Feng, Z. X.; Wang, Z. L.; Zhang, Y. N.; Zhen, C. et al. Three-dimensional Zn-based alloys for dendrite-free aqueous Zn battery in dual-cation electrolytes. *Nat. Commun.* **2022**, *13*, 7922.

[5] Yang, Q.; Li, Q.; Liu, Z. X.; Wang, D. H.; Guo, Y.; Li, X. L.; Tang, Y. C.; Li, H. F.; Dong, B. B.; Zhi, C. Y. Dendrites in Zn-based batteries. *Adv. Mater.* **2020**, *32*, 2001854.

[6] Jiao, Y. D.; Li, F. Y.; Jin, X.; Lei, Q. S.; Li, L. H.; Wang, L.; Ye, T. T.; He, E.; Wang, J. C.; Chen, H. et al. Engineering polymer glue towards 90% zinc utilization for 1000 hours to make high-performance Zn-ion batteries. *Adv. Funct. Mater.* **2021**, *31*, 2107652.

[7] Li, M.; Lu, J.; Chen, Z. W.; Amine, K. 30 years of lithium-ion batteries. *Adv. Mater.* **2018**, *30*, 1800561.

[8] Goodenough, J. B.; Park, K. S. The Li-ion rechargeable battery: A perspective. *J. Am. Chem. Soc.* **2013**, *135*, 1167–1176.

[9] Tarascon, J. M.; Armand, M. Issues and challenges facing rechargeable lithium batteries. *Nature* **2001**, *414*, 359–367.

[10] Tian, Y.; An, Y. L.; Wei, C. L.; Xi, B. J.; Xiong, S. L.; Feng, J. K.; Qian, Y. T. Recent advances and perspectives of Zn-metal free "rocking-chair"-type Zn-ion batteries. *Adv. Energy Mater.* **2021**, *11*, 2002529.

[11] Bai, Y. C.; Zhang, H.; Liang, W. H.; Zhu, C.; Yan, L. J.; Li, C. M. Advances of Zn metal-free "rocking-chair"-type zinc ion batteries: Recent developments and future perspectives. *Small* **2024**, *20*, 2306111.

[12] Li, L.; Jia, S. F.; Cao, M. H.; Ji, Y. Q.; Qiu, H. W.; Zhang, D.

Research progress of “rocking chair” type zinc-ion batteries with zinc metal-free anodes. *Chin. Chem. Lett.* **2023**, *34*, 108307.
[13] Tian, G. F.; Ling, D. D.; Chen, Z.; Zhang, D. H.; Wang, Q. F. Effective CuO/Cu_7S_4 nanospheres heterostructures for advanced “rocking-chair” zinc-ion battery. *J. Colloid Interface Sci.* **2025**, *679*, 334–343.
[14] Qian, Y. Z.; Wang, H. R.; Li, X. N.; Song, T.; Pei, Y.; Liu, L.; Long, B.; Wu, X. W.; Wang, X. Y. Sn-doped BiOCl nanosheet with synergistic H^+/Zn^{2+} co-insertion for “rocking chair” zinc-ion battery. *J. Energy Chem.* **2023**, *81*, 623–632.
[15] Chen, M. L.; He, X.; Zhou, M.; Ning, J.; Zhang, Z. D.; Cao, S. L.; Wang, T. Q.; Wang, K. L.; Jiang, K. Boosting the proton intercalation via crystal plane optimization of TiS_2 for cycling-stable aqueous Zn-ion batteries. *Adv. Energy Mater.* **2024**, *14*, 2400724.
[16] Cao, J.; Zhang, D. D.; Yue, Y. L.; Wang, X.; Srikhaow, A.; Sriprachuabwong, C.; Tuantranont, A.; Zhang, X. Y.; Wu, Z. S.; Qin, J. Q. Strongly coupled tungsten oxide/carbide heterogeneous hybrid for ultrastable aqueous rocking‐chair zinc-ion batteries. *Chem. Eng. J.* **2021**, *426*, 131893.
[17] Chen, R. N.; Li, J. X.; Zhang, D. H.; Zhou, T.; Wu, H.; Wang, Q. F. Revealing the role of topotactic anion exchange in the robust Zn ion storage of $CuS_{1-x}Te_x$. *ACS Sustainable Chem. Eng.* **2025**, *13*, 8164–8172.
[18] Li, W.; Wang, K. L.; Cheng, S. J.; Jiang, K. An ultrastable presodiated titanium disulfide anode for aqueous “rocking-chair” zinc ion battery. *Adv. Energy Mater.* **2019**, *9*, 1900993.
[19] Hou, Y. X.; Chen, S. Y.; Ma, P. F.; Mao, K.; Shi, J. J.; Long, F.; Su, J.; Ma, Y. N.; Gao, Y. H. MXene-derived titanic acid with an ultralow-potential as a promising anode for aqueous zinc-ion batteries. *J. Alloys Compd.* **2023**, *938*, 168714.
[20] Liu, Y.; Zhou, X. M.; Wang, X.; Chen, G. R.; Liu, R.; Ma, Y.; Bai, Y.; Yuan, G. H. Hydrated titanic acid as an ultralow-potential anode for aqueous zinc-ion full batteries. *Chem. Eng. J.* **2021**, *420*, 129629.
[21] Deng, W. J.; Huang, Z. Y.; Zhou, Z. Q.; Li, C.; Chen, Y.; Zhou, Y.; Huang, C.; Zhu, J. L.; Zou, W. X.; Zhu, R. D. et al. A near 0 V and low-strain intercalative anode for aqueous zinc-ion batteries. *ACS Energy Lett.* **2023**, *8*, 3171–3179.
[22] Guo, X. Y.; Li, C.; Zhou, Y.; Chen, Y.; Deng, W. J.; Li, R. $Ti_2O_3(H_2PO_4)_2{\cdot}2H_2O$ as a novel intercalated anode for ultralong lifespan “rocking-chair” aqueous zinc-ion batteries. *Angew. Chem., Int. Ed.* **2025**, *64*, e202502446.
[23] Yang, J.; Li, D.; Wang, X.; Yang, X. J.; Lu, L. D. Study on the synthesis and ion-exchange properties of layered titanate $Na_2Ti_3O_7$ powders with different sizes. *J. Mater. Sci.* **2003**, *38*, 2907–2911.
[24] Kataoka, K.; Kijima, N.; Akimoto, J. Ion-exchange synthesis, crystal structure, and physical properties of hydrogen titanium oxide $H_2Ti_3O_7$. *Inorg. Chem.* **2013**, *52*, 13861–13864.
[25] Wei, M. D.; Wei, K. W.; Ichihara, M.; Zhou, H. S. High rate performances of hydrogen titanate nanowires electrodes. *Electrochem. Commun.* **2008**, *10*, 1164–1167.
[26] Panda, M. R.; Kathribail, A. R.; Modak, B.; Sau, S.; Dutta, D. P.; Mitra, S. Electrochemical properties of biomass-derived carbon and its composite along with $Na_2Ti_3O_7$ as potential high-performance anodes for Na-ion and Li-ion batteries. *Electrochim. Acta* **2021**, *392*, 139026.
[27] Wang, Y. F.; Yu, H. T.; Yi, T. F.; He, F.; Xie, Y. Sea urchins like $Na_2Ti_3O_7$ as long cycling and high-rate performance anodes for Li-ion batteries. *Mater. Chem. Phys.* **2023**, *298*, 127448.
[28] Su, F. L.; Dai, K. S.; Kang, Y. M.; Shui, M.; Shu, J. $Na_2Ti_3O_7$/C rods synthesized by modified sol–gel method as an anode material for sodium ion batteries and the revelation of Na^+ intercalation, diffusion mechanism. *Ionics* **2023**, *29*, 4001–4012.
[29] Byeon, S. H.; Lee, S. O.; Kim, H. Structure and Raman spectra of layered titanium oxides. *J. Solid State Chem.* **1997**, *130*, 110–116.
[30] Fleischmann, S.; Sun, Y. Y. L.; Osti, N. C.; Wang, R. C.; Mamontov, E.; Jiang, D. E.; Augustyn, V. Interlayer separation in hydrogen titanates enables electrochemical proton intercalation. *J. Mater. Chem. A* **2020**, *8*, 412–421.
[31] Saeed, S.; Fleischmann, S.; Kobayashi, T.; Jusys, Z.; Mamontov, E.; Osti, N. C.; Holzapfel, N. P.; Song, H. H.; Wang, T.; Dai, S. et al. Oxide acidity modulates structural transformations in hydrogen titanates during electrochemical Li-ion insertion. *J. Am. Chem. Soc.* **2024**, *146*, 28795–28808.
[32] Li, W.; Ma, Y. S.; Li, P.; Jing, X. Y.; Jiang, K.; Wang, D. H. Electrochemically activated $Cu_{2-x}Te$ as an ultraflat discharge plateau, low reaction potential, and stable anode material for aqueous Zn-ion half and full batteries. *Adv. Energy Mater.* **2021**, *11*, 2102607.
[33] Wang, B.; Yan, J. P.; Zhang, Y. F.; Ye, M. H.; Yang, Y.; Li, C. C. *In situ* carbon insertion in laminated molybdenum dioxide by interlayer engineering toward ultrastable “rocking-chair” zinc-ion batteries. *Adv. Funct. Mater.* **2021**, *31*, 2102827.
[34] Yang, Y.; Xiao, J. F.; Cai, J. Y.; Wang, G. M.; Du, W. C.; Zhang, Y. F.; Lu, X. H.; Li, C. C. Mixed-valence copper selenide as an anode for ultralong lifespan rocking-chair Zn-ion batteries: An insight into its intercalation/extraction kinetics and charge storage mechanism. *Adv. Funct. Mater.* **2021**, *31*, 2005092.
[35] Yan, L. J.; Zeng, X. M.; Li, Z. H.; Meng, X. J.; Wei, D.; Liu, T. F.; Ling, M.; Lin, Z.; Liang, C. D. An innovation: Dendrite free quinone paired with $ZnMn_2O_4$ for zinc ion storage. *Mater. Today Energy* **2019**, *13*, 323–330.
[36] Deng, W. J.; Zhou, Z. Q.; Li, Y. B.; Zhang, M.; Yuan, X. R.; Hu, J.; Li, Z. G.; Li, C.; Li, R. High-capacity layered magnesium vanadate with concentrated gel electrolyte toward high-performance and wide-temperature zinc-ion battery. *ACS Nano* **2020**, *14*, 15776–15785.
[37] Liu, X.; Euchner, H.; Zarrabeitia, M.; Gao, X. P.; Elia, G. A.; Groß, A.; Passerini, S. *Operando* pH measurements decipher H^+/Zn^{2+} intercalation chemistry in high-performance aqueous $Zn/\delta\text{-}V_2O_5$ batteries. *ACS Energy Lett.* **2020**, *5*, 2979–2986.
[38] Oberholzer, P.; Tervoort, E.; Bouzid, A.; Pasquarello, A.; Kundu, D. Oxide versus nonoxide cathode materials for aqueous Zn batteries: An insight into the charge storage mechanism and consequences thereof. *ACS Appl. Mater. Interfaces* **2019**, *11*, 674–682.
[39] Rydh, C. J. Environmental assessment of vanadium redox and lead-acid batteries for stationary energy storage. *J. Power Sources* **1999**, *80*, 21–29.
[40] Palacín, M. R.; de Guibert, A. Why do batteries fail. *Science* **2016**, *351*, 1253292.
[41] Luo, J. Y.; Cui, W. J.; He, P.; Xia, Y. Y. Raising the cycling stability of aqueous lithium-ion batteries by eliminating oxygen in the electrolyte. *Nat. Chem.* **2010**, *2*, 760–765.
[42] Suo, L. M.; Borodin, O.; Gao, T.; Olguin, M.; Ho, J.; Fan, X. L.; Luo, C.; Wang, C. S.; Xu, K. “Water-in-salt” electrolyte enables high-voltage aqueous lithium-ion chemistries. *Science* **2015**, *350*, 938–943.
[43] Weng, G. M.; Simon Tam, L. Y.; Lu, Y. C. High-performance $LiTi_2(PO_4)_3$ anodes for high-areal-capacity flexible aqueous lithium-ion batteries. *J. Mater. Chem. A* **2017**, *5*, 11764–11771.
[44] Shao, M. M.; Deng, J. T.; Zhong, F. P.; Cao, Y. L.; Ai, X. P.; Qian, J. F.; Yang, H. X. An all-vanadium aqueous lithium ion battery with high energy density and long lifespan. *Energy Storage Mater.* **2019**, *18*, 92–99.
[45] Wang, F. X.; Jiang, Q. K.; Song, Z. H.; Liu, S. S.; Feng, K.; Yang, X.; Cao, Z. B.; Jia, J. S.; Zhang, H. Z. A rational designed high-rate $Cu_xTi_2(PO_4)_3$@Cu/C core-composite-shell structure for aqueous lithium ion batteries. *J. Power Sources* **2020**, *468*, 228248.
[46] Jaumaux, P.; Yang, X.; Zhang, B.; Safaei, J.; Tang, X.; Zhou, D.; Wang, C. S.; Wang, G. X. Localized water-in-salt electrolyte for aqueous lithium-ion batteries. *Angew. Chem., Int. Ed.* **2021**, *60*, 19965–19973.
[47] Zhu, R. D.; Deng, W. J.; Li, C.; Zhou, Y.; Zhu, J. L.; Huang, C.; Xu, Y. S.; Zou, W. X.; Li, R. Layered titanium phosphate nanosheets with water in salt electrolyte toward high-voltage aqueous full lithium-ion batteries. *New J. Chem.* **2024**, *48*, 7779–7784.

[48] Jin, T.; Ji, X.; Wang, P. F.; Zhu, K. J.; Zhang, J. X.; Cao, L. S.; Chen, L.; Cui, C. Y.; Deng, T.; Liu, S. F. et al. High-energy aqueous sodium-ion batteries. *Angew. Chem., Int. Ed.* **2021**, *60*, 11943–11948.

[49] Liang, Z. H.; Tian, F.; Yang, G. Z.; Wang, C. X. Enabling long-cycling aqueous sodium-ion batteries via Mn dissolution inhibition using sodium ferrocyanide electrolyte additive. *Nat. Commun.* **2023**, *14*, 3591.

[50] Meng, Q. Y.; Shao, J. C.; Dou, X. R.; Chi, H. Z. N-containing $Na_2VTi(PO_4)_3$/C for aqueous sodium-ion batteries. *Small* **2024**, *20*, 2308483.

[51] Vardhini, G.; Dilip, P. S.; Kumar, S. A.; Suriyakumar, S.; Hariharan, M.; Shaijumon, M. M. Polyimide-based aqueous potassium energy storage systems using concentrated WiSE electrolyte. *ACS Appl. Mater. Interfaces* **2024**, *16*, 48782–48791.

[52] Zeng, G. W.; Ali, U.; Sun, M. Y.; Zhang, Y.; Fu, L. H.; Li, Y. Q.; Hao, Y. H.; Liu, B. Q.; Wang, C. G. Intercalation pseudocapacitance mechanism realizes high-performance cathode for aqueous potassium ion batteries. *J. Colloid Interface Sci.* **2024**, *653*, 46–55.

[53] Zeng, G. W.; Liu, B. Q.; Ali, U.; Li, Y. X.; Jia, H. F.; Sun, M. Y.; Li, Y. Q.; Hao, Y. H.; Yong, X.; Wang, T. T. et al. The local disorder induced by high-entropy doping results in highly stable cathode materials for aqueous potassium-ion batteries. *Appl. Catal. B: Environ. Energy* **2024**, *351*, 123996.

[54] Liu, B. Q.; Zhang, Q.; Yu, X. Y.; Feng, Y. T.; Yang, Z.; Zhou, W. H.; Xie, D.; Li, C. Y.; Chen, Y. J.; Li, L. et al. Unlocking polyanion-type materials through high-entropy effect for aqueous potassium-ion batteries. *J. Am. Chem. Soc.* **2025**, *147*, 38291–38300.

[55] Tan, X.; Gao, C. Y.; Luo, Z. F.; Fan, W. J.; Xiong, X. S.; Shi, Z. Z.; Zhang, N. X.; Yang, Z.; Ma, Y.; Cheng, X. B. et al. Unveiling aqueous potassium-ion batteries with Prussian blue analogue cathodes. *Small* **2025**, *21*, 2410350.

[56] Jiang, H.; Shin, W.; Ma, L.; Hong, J. J.; Wei, Z. X.; Liu, Y.; Zhang, S. Y.; Wu, X. Y.; Xu, Y. K.; Guo, Q. B. et al. A high-rate aqueous proton battery delivering power below −78 °C via an unfrozen phosphoric acid. *Adv. Energy Mater.* **2020**, *10*, 2000968.

[57] Qiao, J.; Qin, M.; Shen, Y. M.; Cao, J. Y.; Chen, Z. D.; Xu, J. A rechargeable aqueous proton battery based on a dipyridophenazine anode and an indium hexacyanoferrate cathode. *Chem. Commun.* **2021**, *57*, 4307–4310.

[58] Tong, Y. H.; Wei, Y.; Song, A. J.; Ma, Y. Y.; Yang, J. P. Polyaniline/tungsten trioxide organic-inorganic hybrid anode for aqueous proton batteries. *Chem.—Eur. J.* **2024**, *30*, e202401257.

[59] Wu, S. C.; Taylor, M.; Guo, H. C.; Wang, S. H.; Han, C.; Vongsvivut, J.; Meyer, Q.; Sun, Q.; Ho, J.; Zhao, C. A high-capacity benzoquinone derivative anode for all-organic long-cycle aqueous proton batteries. *Angew. Chem., Int. Ed.* **2024**, *63*, e202412455.

[60] Barnwal, N.; Pravarthana, D. Topochemical copper nitroprusside cathode enables high capacity and cyclability aqueous proton batteries. *ACS Appl. Energy Mater.* **2025**, *8*, 16852–16860.

[61] Wu, Z. R.; Li, Y. H.; Liu, J. Coulombic efficiency for practical zinc metal batteries: Critical analysis and perspectives. *Small Methods* **2024**, *8*, 2300660.

[62] Ju, Z. N.; Zhao, Q.; Chao, D. L.; Hou, Y.; Pan, H. G.; Sun, W. P.; Yuan, Z. Y.; Li, H.; Ma, T. Y.; Su, D. W. et al. Energetic aqueous batteries. *Adv. Energy Mater.* **2022**, *12*, 2201074.